Research Article | Vol. 13, No. 1 / 1 Jan 2023 / Optical Materials Express 9
Optical Materials EXPRESS

Plasmonic nanoresonator distributions for uniform energy deposition in active targets

DÁVID VASS,[1,2] ANDRÁS SZENES,[1,2] EMESE TÓTH,[1,2] BALÁZS BÁNHELYI,[1,2,3] ISTVÁN PAPP,[2,4] TAMÁS BÍRÓ,[2] LÁSZLÓ P. CSERNAI,[2,4,5] NORBERT KROÓ,[2,6] AND MÁRIA CSETE[1,2,*]

[1]*University of Szeged, Department of Optics and Quantum Electronics, Szeged 6720, Hungary*
[2]*Wigner Research Centre for Physics, Budapest 1121, Hungary*
[3]*University of Szeged, Department of Computational Optimization, Szeged 6720, Hungary*
[4]*University of Bergen, Department of Physics and Technology, Bergen 5007, Norway*
[5]*Frankfurt Institute for Advanced Studies, Frankfurt/Main 60438, Germany*
[6]*Hungarian Academy of Sciences, Budapest 1051, Hungary*
[*]*mcsete@physx.u-szeged.hu*

Abstract: Active targets implanted with core-shell-composition (CS) and nanorod-shaped (NR) plasmonic nanoresonators and doped with dyes were designed to ensure uniform energy deposition during illumination by two-counter propagating short laser pulses. The near-field enhancement, optical responses, and cross-sections were mapped above the concentration-E_{pump} parameter-plane to inspect two different regions (I and II) with the potential to improve light-matter interaction phenomena. The distribution of steady-state absorption, as well as of the power-loss and power-loss density integrated until the complete overlap of the two short pulses was determined. The uniform distribution was adjusted to constrain standard deviations of the integrated power-loss distributions in the order of ∼10%. Dye doping of target-I/II implanted with uniform CS (NR) nanoresonator distributions results in larger absorption with increased standard deviation, larger power-loss, and power-loss density with decreased (decreased / increased) standard deviation. The adjustment allows larger absorption in CS-II and larger power-loss and power-loss density in CS-implanted targets, smaller standard deviation in targets-I for absorption, and in all targets for power-loss and its density. Larger dye concentration makes it possible to achieve larger absorption (except in adjusted NR-II), larger power-loss and power-loss density in all CS and in adjusted NR distributions, with decreased standard deviation in CS-implanted targets for all quantities and in NR-implanted targets for absorption. CS implantation results in larger absorption with a larger standard deviation, moreover allows larger power-loss in adjusted distributions and smaller standard deviation in power-loss quantities for larger concentration in both distributions and the same standard deviation for smaller concentration in adjusted distribution. Based on these results, adjusted CS distributions in targets doped with a dye of higher concentration are proposed.

© 2022 Optica Publishing Group under the terms of the Optica Open Access Publishing Agreement

1. Introduction

Nuclear power and hydrogen nuclear fusion reaction is a potential candidate to solve the energy demand, however a safe and sustainable hydrogen nuclear fusion reaction technology has not been demonstrated yet [1]. Earlier studies suggested the application of nanophotonics to promote laser beam penetration into targets and to prevent the plasma mirror problem by applying e.g. nanowires that make it possible to reach electron densities nearly 100-times greater than the typical critical density [2]. Short (35 fs) laser induced surface structures (LIPSS), created by the interference of the laser light and surface plasmon polaritons, can be used to boost the proton acceleration and to improve the proton cut-off energy and conversion efficiency [3,4].

#471980 https://doi.org/10.1364/OME.471980
Journal © 2023 Received 1 Aug 2022; revised 26 Sep 2022; accepted 28 Sep 2022; published 6 Dec 2022

Optical Materials EXPRESS

Two-dimensional 250 nm periodic hexagonal array of silver nanowires with 400 nm height embedded into an alumina matrix were designed to promote high power laser (532 nm, 9 ns, 4×10^{12} W/cm^2) induced D-D fusion inside the alumina pores on the top of nanowires that can be filled-up with a deuterium-doped oxide [5]. Enormous **E**-field enhancement ($\sim 2 \times 10^8$) on high aspect ratio (100 and 1000) nano-objects made of hydrogen absorbing transition metals (Pd, Ti, Ni,) due to lightening rod effect was demonstrated in the microwave region (1-10 μm) and suggested to improve hydrogen related devices' performance [6].

The application of resonant noble metallic materials is also promising in target designs. Metal nanoparticles are capable of sustaining collective electron plasma oscillations nominated as localized surface plasmon resonance (LSPR), which can be resonantly excited by polarized light. In the vicinity of nanoparticles, the electromagnetic field is confined into a range comparable with that of the particle size [7]. LSPRs are lossy oscillations caused by radiation escape via scattering on the particle and heat loss in the metal. The resonance frequency, decay rate as well as the absorption and scattering ratio can be modified by varying the particle size, shape or the environment on demand [8]. The frequency of plasmonic resonance as well as the decay rate related to radiative and ohmic losses can be engineered on nanorods (NRs) via aspect ratio (AR) tailoring. Transversal and longitudinal plasmon resonance can be excited in case of **E**-field oscillation along the short and long axes, respectively [9]. Therefore, the achievable near-field enhancement and absorption depend significantly on the relative orientation of the polarization of the incident light and the nanorods [10]. Nanorod distributions embedded into targets were proposed for various application purposes requiring tuneable light absorption, localization of electromagnetic fields and photothermal conversion. In such distributions, the randomly oriented nanorods may interact with each other in dense arrangements [11]. LSPRs can be excited on dielectric-metal core-shell nanoparticles as well, due to the hybridization of elementary plasmons, i.e. interaction of primitive sphere and cavity plasmons. The strength of this interaction depends on the thickness of the metal shell, the order of the involved sphere and cavity plasmons and the type of hybridization [12]. The size parameter used to tune all these components is the generalized aspect ratio (GAR = R_{in}/R_{out} ratio of the inner and outer radius). By varying GAR the resonance wavelength of the hybridized modes can be tuned in a wide spectral range, i.e from the visible spectra up to the infrared region [13].

There are versatile applications of the enhancement achievable via implanted plasmonic particles. The application of near-infrared (NIR) fs laser illumination of plasmonic nanoparticles in cancer treatment and drug delivery was proposed based on the possibility to induce bond breaking during a single-particle phenomenon without heating effects due to the short interaction time-scale [14]. The existence of optimal nanorod aspect ratio for cellular uptake and temperature increase control in fs laser driven in vivo tissue treatments was demonstrated [15]. It was shown that when plasmonic nanoparticles are delivered to cancer tissues to locally increase the temperature and to damage the cancer cell using light exposure in plasmonic photothermal therapy of cancer (PPTT), where the metal amount, nanoparticle size and light-to-heat conversion are the critical parameters [16].

Nanoparticles can enhance the spontaneous emission of nearby emitters, since the total decay rate increases due to the large local density of optical states (LDOS) during LSPR that is accompanied by large near-field enhancement [17]. The luminescence of organic dye molecules can be significantly enhanced by plasmonic nanoparticles, enabling the preparation of novel efficient light-emitting devices, moreover leading to nanoscale lasing [18]. Particular advantage of nanorods is that the field strength can be very high at the apexes due to the small radius of curvature, making them suitable for applications that require the presence of intense hotspots, such as surface enhanced Raman spectroscopy and nanolasers [19].

Optical Materials EXPRESS

In specific types of plasmonic lasers nominated as spasers the plasmonic modes accompanying the LSPR of metallic nanoresonators ensure the feedback. The coherent control was proposed to tailor the spaser threshold, frequency, number of involved plasmons as well as the dynamics [20].

Spaser operation was first demonstrated experimentally with a dielectric layer containing a four-level organic dye as an active medium around a spherical gold nanoparticle [21]. For small metal nanoparticles the minimal spasing threshold is governed by the material properties, for larger particles the scattering losses can increase this threshold. The minimal threshold inherits the features of material dispersion, which results in extrema in all optical responses at specific wavelengths [22]. The entering into spasing operation region is accompanied by negative extinction cross-section [22,23].

An important application area of plasmonic particles is the development of coherent light sources that facilitate ultra-strong light-matter interaction at the nanoscale [24]. The potential of nanolasers to achieve high optical energy densities by simultaneous spatial, temporal and spectral confinement opens novel avenues in ultra-strong light-matter interactions [25]. The spectral hole-burning effect demonstrated on 35 fs (800 nm) laser illuminated plasmonic nanorods proved that the plasmonic effect holds up to extreme fluences and allows plasmonic enhancement at the level of 10^6 J/m^2 (1.5×10^{11} V/m) [26]. The dynamics of plasmonic oscillations on resonant antennae follow the intense driving field cycles during short pulse illumination [27]. Random distributions of plasmonic nanospheres and nanorods covered with rhodamine B (RhB) dye provided excitation enhancement, altered the radiative rate, scattered the emitted light more efficiently, resulted in a linewidth narrowing and increased the effective emission rate [28]. The possibility to control the pump threshold, the evolution of spikes and the involved modes in random lasing media containing dyes via optimized metal-silica core-shell structures was demonstrated [29]. The principle of combining a spaser and random laser operation was proposed, and control parameters as the number density to tailor the mean scattering free path, the optimal coating to avoid non-radiative losses, the optimal geometries to enhance both excitation and emission were identified [30]. In various light-matter interaction phenomena inside extended targets, e.g. fabrication, surgery, cancer treatment, drug delivery, spontaneous and stimulated emission enhancement, it is crucial to balance the distribution of the absorbed power and deposited energy (as well as their densities). Moreover, in high-power pulsed laser applications the full control of the time-evolution of theses quantities ensures the optimal ultra-strong light-matter interaction. In case of critical phenomena, e.g. time-like ignition in fusion, the four-dimensional control of the light-matter interaction is necessary to reach the threshold **E**-field strength throughout extended targets uniformly.

There are several examples in the literature that suggest to apply resonant plasmonic particles in laser driven fusion targets [31–35]. In our previous studies we have inspected the possibility of plasmonic enhancement and of energy deposition balancing in extended passive targets implanted with nanoresonators [35]. The idea of present study is that by embedding the same type of plasmonic nanoresonators, e.g. nanorods and core-shell nanoparticles, into active dye doped media, the local E-field enhancement might be boosted and novel degrees of freedom open that allow more efficient and uniform deposition of larger amount of energy in active plasmonic targets. The optical response of the nanoresonators and nanophotonical phenomena behind are studied, while the surrounding active medium is considered as a kind of a pre-designed capsule that facilitates to achieve the desired effects.

2. Methods

The individual nanoresonators' geometry was tuned to ensure plasmonic resonance at the 795 nm central wavelength of the 120 fs short pulse. Uniform distributions of nanoresonators with core-shell (CS) composition and nanorod (NR) shape were then inspected. Namely, the CS-targets were implanted with 70 resonant silica-gold core-shell nanoparticles and 70 gold

Optical Materials EXPRESS

nanorods were embedded into NR-targets, that correspond to 3.33×10^{12} cm^{-3} number density. Beside the passive ones, active targets doped with laser dye (LDS 798 or Styryl 11) were also studied. Modelling of the dye response was realized with coupled rate equations to determine the effect of the 795 nm probe pulse, by considering different pump field-strengths (E_{pump}) of 532 nm wavelength and by using the method described in our previous paper [23].

The local field strengths achieved at the highest inspected E_{pump} are below the damage threshold of similar gold nanoparticles at 532 nm, even in case of ns pulsed illumination [36]. The power density (corresponding to 10^4 V/m **E**-field strength) of the probe beam was far below the damage threshold for short pulses of ~800 nm central wavelength found in the literature [37,38], it was selected according to the usual pump-and-probe scenario and to avoid entering into nonlinear regions in the enhanced local fields that would require application of hydrodynamic models, which is time-consuming in extended targets [39].

The available **E**-field enhancement, optical responses and cross-sections above the pump **E**-field strength (E_{pump}) and dye concentration (c) parameter-plane were mapped to determine regions of large plasmonic enhancements (Fig. 1,2/a-d). The near-field and far-field responses determined by steady-state computations were inspected to identify (E_{pump}, c) parameter regions more suitable for local **E**-field enhancements at the probe wavelength. Comparison of two representative parameter regions corresponding to local and global extrema in the **E**-field enhancement around the nanoresonators was performed rather than those corresponding to extrema in gold absorptance or absorption cross-section. This can be explained by that the **E**-field strength determines the interaction with the surrounding material, e.g. the doping dye. Accordingly, inspection of the average and maximal near-field enhancements around the nanoresonators, absorption of gold nanoresonators and dye doped polymer targets acting as a gain media, the outflow, as well as the absorption (ACS, including only the gold nanoresonators, gain medium or both material segments), scattering (SCS) and extinction (ECS) cross-sections was realized around two representative extrema in the $\mathbf{E}_{max}$ above the (E_{pump}, c) parameter plane, similarly to our previous studies on singlet nanoresonators [23].

Namely, at two selected dye concentrations (nominated as type-I and type-II) in the surrounding active medium the pump dependence was studied in more detail (Fig. 1,2(e)-(h)). The CS-I and NR-I is doped with dye of smaller concentration (5×10^{25} m^{-3} and 2×10^{25} m^{-3}), whereas CS-II and NR-II are doped with dye of larger concentration (2.25×10^{26} m^{-3} and 2.5×10^{26} m^{-3}). The parallel monitoring of the nanoresonator-volume averaged and maximal **E**-field enhancements attainable around them promotes to eliminate local fluctuations. The absorption, scattering and extinction cross-sections were analyzed to uncover dominant nanophotonical phenomena. Moreover, at the pump resulting in extremum, the spectral responses were also investigated to prove presence of plasmonic resonances (Fig. 1,2(i)-(l)). The steady-state responses of CS and NR were compared to consider the advantages of nanoresonator geometry for specific applications (Fig. 1 to 2).

Beside the absorption determined based on the resistive heating read out in steady-state computations, the time-evolution of the absorbed power and its density (as well as the deposited energy and its density, see Supplement 1), that are the key parameters during ignition of fusion targets, were also inspected [34,35]. These quantities were evaluated by computing the time-dependent resistive heating in the nanoresonators (as well as in the gain medium and inside the complete target, not shown) in seven consecutive layers of the passive and active targets via time-domain computations. The power-loss and power-loss density distributions (as well as the energy and energy density distributions, see Supplement 1), were subsequently integrated until the complete overlap of two counter-propagating 120 fs probe pulses (Fig. 3 and 4). Finally, the nanoresonator distributions were adjusted in order to constrain the normalized standard deviations of integrated power-loss distributions along the targets in the order of ~10%. This standard deviation constraint could be further reduced on demand.

Optical Materials EXPRESS

The effect of dye doping at smaller (type-I) or larger (type-II) concentration and nanoresonator number density distribution adjustment was analyzed, and the advantages of two different distributions, dye concentrations and two different nanoresonator geometries were compared in order to conclude about the most suitable active target configuration. In this study the quantities extracted for the plasmonic nanoresonators were analyzed, by considering the specific application purpose that requires uniform and large non-radiative, i.e. absorbed power-loss achievement accompanied by large local **E**-field enhancement.

The thermal relaxation of gold containing nanoresonators occurs on a longer timescale, and the heat transfer to the environment that could have impact on dye saturation at larger intensities, was out of the scope of the present study [40].

3. Results and discussion

3.1. *E*-field enhancements

The uniform CS and NR distribution embedded into a passive target causes similar 13-fold and 23-fold increase in the average **E**-field strength, while strong 65-fold and more than two-times stronger 147-fold increase occurs in the maximal **E**-field strength. One-order of magnitude larger average and maximal **E**-field enhancements are achieved both in type-I and type-II active targets than in their corresponding passive counterpart (except in the NR-II, where the moderate enhancement is 2.26-fold in average and 3.16-fold in maximal **E**-field strength), for both nanoresonator geometries (Fig. 1,2(a), (e), see Supplement 1 Table S1, S2).

By comparing NR-I and CS-I targets, in CS-I the maximum achieved in the average **E**-field strength is slightly smaller ($E_{av\_CS-I} = 1.15 \times 10^6$ V/m < $E_{av\_NR-I} = 1.38 \times 10^6$ V/m), and two-times smaller maximum is reached in the maximal **E**-field strength ($E_{max\_CS-I} = 9.43 \times 10^6$ V/m < $E_{max\_NR-I} = 17.8 \times 10^6$ V/m) due to the slightly smaller average (115-fold < 138-fold) and two-times smaller maximal (943-fold << 1780-fold) probe **E**-field enhancement, respectively. Based on the **E**-field enhancements the NR-I target is better at small concentration (Fig. 1,2(a), (e), see Supplement 1 Table S1, S3).

In contrast, by comparing NR-II and CS-II targets, in CS-II more than two-times larger maximum is achieved in the average **E**-field strength ($E_{av-CS-II} = 1.24 \times 10^6$ V/m >> $E_{av-NR-II} = 0.52 \times 10^6$ V/m), and almost two-times larger maximum is observed in the maximal **E**-field strength ($E_{max-CS-II} = 7.81 \times 10^6$ V/m > $E_{max-NR-II} = 4.65 \times 10^6$ V/m) due to the more than two-times larger average (124-fold >> 52-fold) and almost two-times larger maximal (781-fold > 465-fold) probe **E**-field enhancement, respectively. Based on the **E**-field enhancements the CS-II target is better at large concentration (Fig. 1,2(a), (e), Table S1, S3 in Supplement 1).

By comparing type-I and type-II targets, in CS-II the average **E**-field enhancement is slightly larger, but the maximal **E**-field enhancement is slightly smaller, while both quantities are significantly (almost and more than three-times) smaller in case of NR-II. Counter-intuitively, the concentration increase does not result in **E**-field enhancement, except the average **E**-field value in CS-II (Table S3 in Supplement 1).

In the passive targets there is a local (global) maximum in the average and a global (local) maximum in the maximal **E**-field enhancement spectra in case of CS (NR) implantation. In the CS-I target a local maximum appears at the short wavelength side of the global maximum, whereas in CS-II target the local maximum that is shifted to shorter wavelengths is well separated from the global maximum, and an additional tiny neighboring maximum appears at slightly larger wavelength in the **E**-field enhancement spectra. In NR-I target a single wide global maximum appears both in the average and maximal **E**-field spectra, whereas in the NR-II target two side-peaks similar to those in CS-II / multiple peaks appear in the average /maximal **E**-field spectrum. The enhancement is smaller (larger) in the average (maximal) **E**-field in all inspected targets (Fig. 1,2(i)).

Optical Materials EXPRESS

In all inspected targets the local **E**-field enhancement has unambiguously a plasmonic origin, that can be further improved by dye doping. At the emission, the field enhancement takes on one order of magnitude larger global maximum in the average and maximal **E**-field at both concentrations of the dye compared to the passive target (except the NR-II) (Fig. 1,2(a),(e),(i), Table S1-S3 in Supplement 1). The maximum **E**-field enhancement is larger in case of lower dye concentration independent of nanoresonator geometry. Larger average **E**-field enhancement is achieved at higher (lower) concentration in case of CS (NR) implantation.

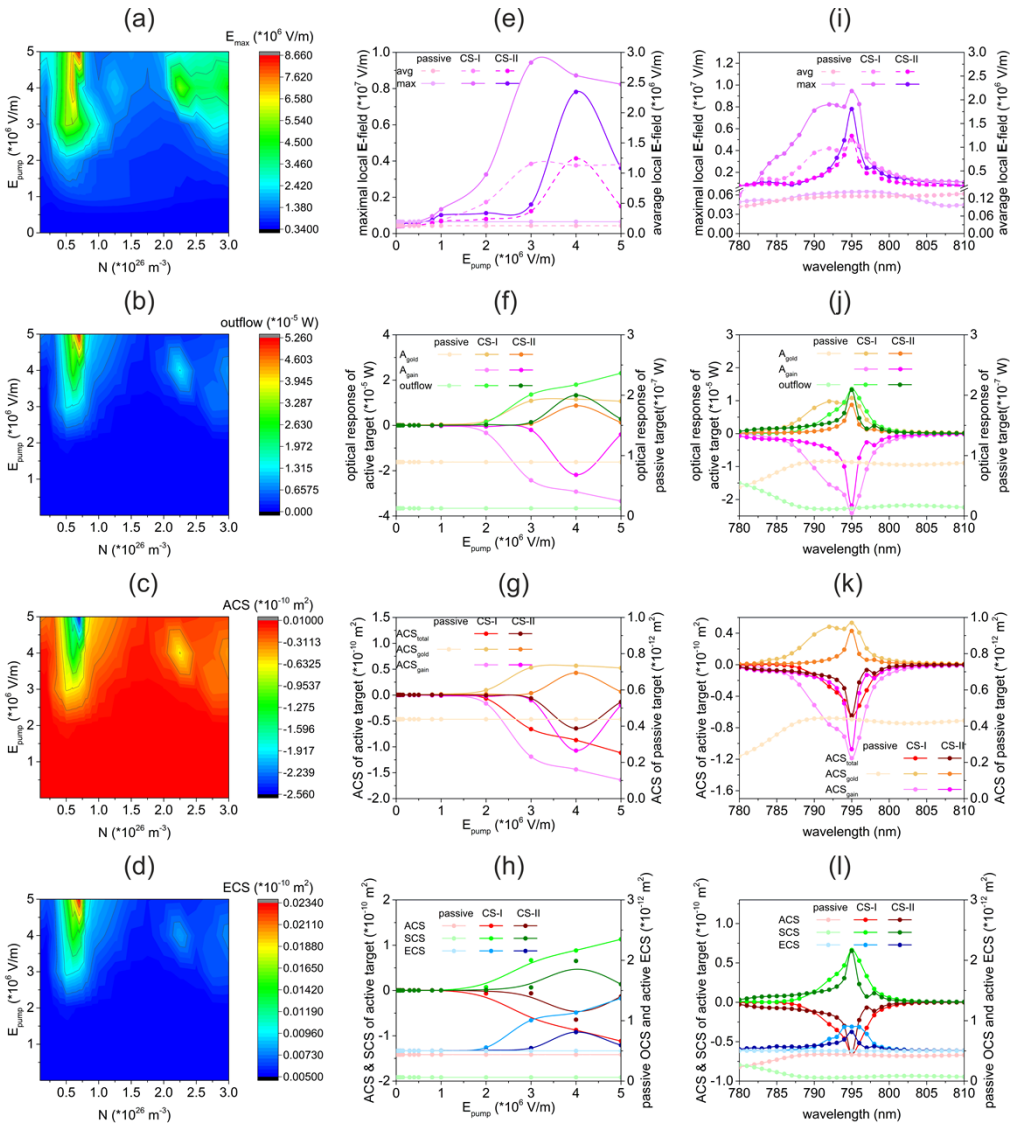

Fig. 1. Steady-state responses of the uniform CS nanoresonator distribution in passive and active targets. The (a) maximal local **E**-field of the probe, (b) outflow, (c) ACS and (d) ECS above the $\mathbf{E}_{\text{pump}}$-concentration parameter-plane, the pump/wavelength dependence of the (e/i) local **E**-field, (f/j) the optical response, the (g/k) different components of ACS and the (h/l) total ACS, SCS, ECS in case of CS implanted targets.

Optical Materials EXPRESS

3.2. Optical responses

The uniform CS and NR distributions in passive targets result in a minor gold absorptance (0.009×10^{-5} W and 0.008×10^{-5} W) and a significantly smaller outflow (0.001×10^{-5} W and 0.002×10^{-5} W). The CS distribution slightly better promotes the absorptance, while the NR distribution allows two-times larger outflow (Fig. 1,2(b), (f), Table S1, S3 in Supplement 1). The absorptance is two- while the outflow is three orders of magnitude larger both in CS-I and CS-II doped active targets, than in their corresponding passive counterpart. In comparison, the absorptance is (almost) two and the outflow is (two) three orders of magnitude larger in (NR-I) NR-II active targets, than in their passive counterpart (Fig. 1,2(b), (f), Table S1, S2 in Supplement 1).

In CS-I and NR-I all tendencies are similar, namely the gold absorptance takes on a maximum, while the absolute value of the emission in gain medium as well as the outflow monotonously increases. By comparing the values at the selected $E_{pump} = 3 \times 10^6$ V/m pump field strength, more than two-times larger absorption and almost two-times larger radiation escape are observable in CS-I compared to NR-I ($A_{gold\_CS-I} = 1.15 \times 10^{-5}$ W > $A_{gold\_NR-I} = 0.47 \times 10^{-5}$ W, $A_{gain\_CS-I} = |-2.42 \times 10^{-5}|$ W > $A_{gain\_NR-I} = |-1.05 \times 10^{-5}|$ W, $Outflow_{\_CS-I} = 1.36 \times 10^{-5}$ W > $Outflow_{\_NR-I} = 0.\ 75 \times 10^{-5}$ W) (Fig. 1,2(b), (f), Table S1, S3 in Supplement 1).

In CS-II and NR-II targets all quantities take on global extrema at the selected 4×10^6 V/m and 3×10^6 V/m pump field strengths, respectively. The slightly larger absorption in gold ($A_{gold\_CS-II} = 0.87 \times 10^{-5}$ W > $A_{gold\_NR-II} = 0.74 \times 10^{-5}$ W) and significantly smaller gain medium emission ($A_{gain\_CS-II} = |-2.18 \times 10^{-5}|$ W << A_{gain_NR-II}: $|-5.52 \times 10^{-5}|$ W) allow significantly smaller outflow ($Outflow_{\_CS-II} = 1.33 \times 10^{-5}$ W < $Outflow_{\_NR-II} = 4.82 \times 10^{-5}$ W) from the CS-II target (Fig. 1,2(b), (f), Table S1, S3 in Supplement 1).

The targets exhibit fundamentally different optical responses at the two dye concentrations. This manifests itself in different tendencies, namely CS-I and NR-I exhibit monotonous optical responses (except the gold absorptance), whereas CS-II and NR-II exhibit global extrema in the optical response at 4×10^6 V/m and 3×10^6 V/m pump field strengths, respectively. Each quantities have smaller values in CS-II than in CS-I, whereas each quantity reach larger values in NR-II than in NR-I. In case of NR the enhancements in the two optical responses are larger (almost two-times for the gold absorption and almost (more than) six-times for the gain (outflow)) for larger concentration compared to the passive target (Fig. 1,2(b), (f), Table S3 in Supplement 1).

In case of CS nanoresonator distribution the absorption is commensurate with the outflow, whereas in case of NR nanoresonator distribution the absorption is (almost two-times and more than six-times) smaller than the outflow for both inspected targets (Fig. 1,2(b), (f), Table S1 in Supplement 1).

A wide maximum appears in the absorptance nearby the emission wavelength of 795 nm, and there is a reversal modulation in the outflow of the passive targets. In the CS-I target a local maximum and a shoulder appears in the gold absorption and in the gain medium emission before the global maximum at 795 nm, that uncovers coupled modes, whose effect is partially hidden in the shoulder preceding the global maximum in the outflow. In CS-II target a smaller global maximum appears in all optical responses at 795 nm neighbored by a tiny side peak at its long-wavelength-side. In NR-I, the gold absorption, gain medium emission and outflow exhibits a single wide global maximum near 795 nm. In NR-II target a larger but narrower global maximum with a preceding local maximum appears in the gain medium emission and outflow (less noticeable in the gold absorption), moreover the global maximum is accompanied by a local maximum at 800 nm in all quantities, again revealing coupled modes (Fig. 1,2(j)).

All active systems result in a considerable optical response enhancement compared to their passive counterpart that is system and quantity specific, but is on the level of orders of magnitude. For both nanoresonator geometries similar switching occurs from monotonous tendencies (except

Optical Materials EXPRESS

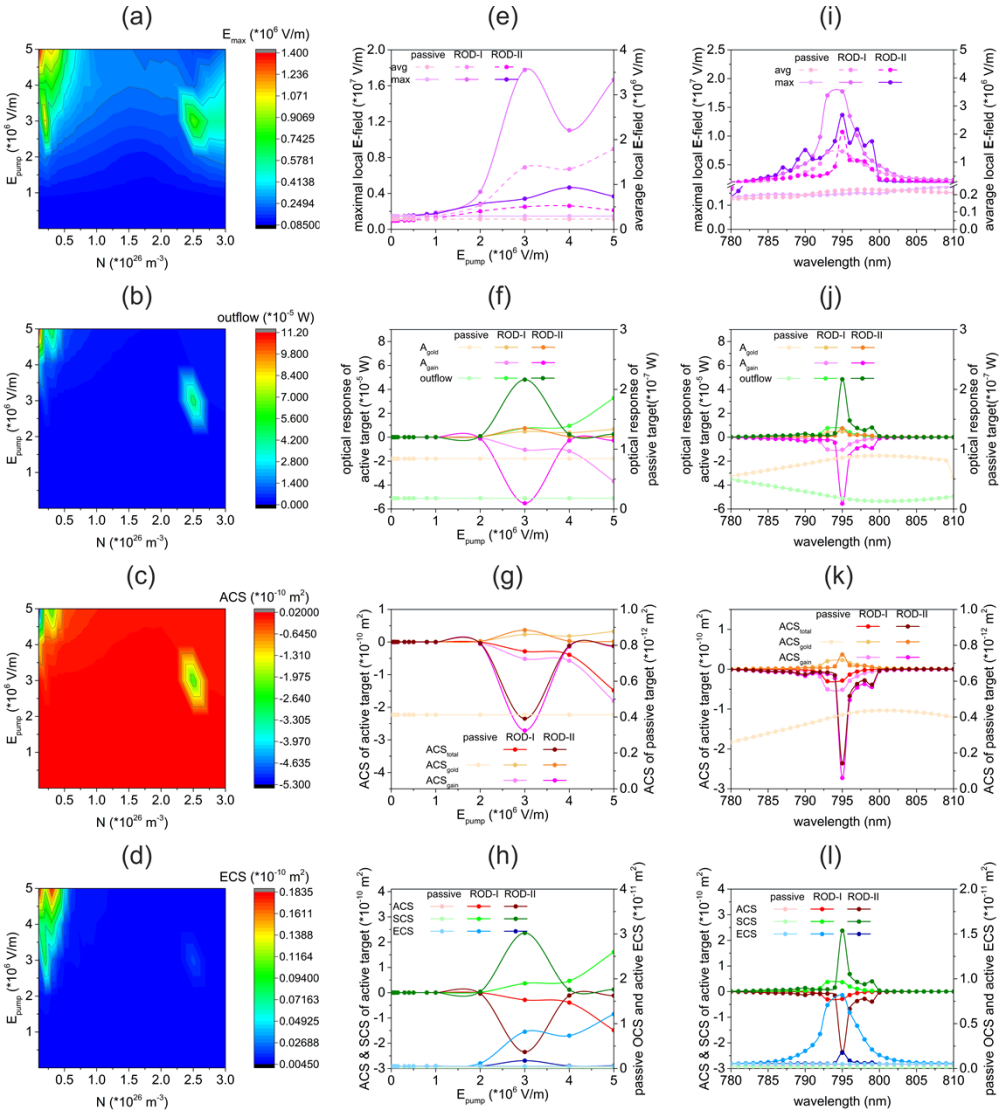

Fig. 2. Steady-state responses of the uniform NR nanoresonator distribution in passive and active targets. The (a) maximal local **E**-field of the probe, (b) outflow, (c) ACS and (d) ECS above the $\mathbf{E}_{\text{pump}}$-concentration parameter-plane, the pump/wavelength dependence of the (e/i) local **E**-field, (f/j) the optical response, the (g/k) different components of ACS and the (h/l) total ACS, SCS, ECS in case of NR implanted targets.

the gold absorptance) in target-I to global extrema in target-II. CS-II target allows slightly smaller, while NR-II target allows considerably larger enhancements than their type-I counterparts. In the spectrum of all inspected targets a global absorptance maximum appears at 795 nm that proves a properly tuned plasmonic resonance that is accompanied by a global maximum in the gain medium emission and outflow.

In case of CS implanted targets the smaller concentration (CS-I target), whereas in case of the NR implanted targets the larger concentration (NR-II) facilitates larger number of additional modes coupling that more significantly broadens the collective spectral responses (Fig. 1,2(b),(f),(j),

Optical Materials EXPRESS

Table S1-S3 in Supplement 1). However, spectral broadening is not spurious in case of short pulse illumination, on the contrary, broader gold absorption of randomly distributed nanoresonators promote the non-radiative losses in wider spectral interval.

3.3. Optical cross-sections

The uniform CS and NR nanoresonator distribution in passive targets results in tiny and E_{pump} independent optical cross-sections (ACS: 0.004×10^{-10} m^2, SCS: 0.001×10^{-10} m^2, ECS: 0.005×10^{-10} m^2), the resistive loss in gold nanoresonators completely determines the total absorption cross-section, and the tiny positive ECS is governed by the ACS rather than by the SCS, indicating small radiative losses (Fig. 1,2(c),(g),(k) and (d),(h),(l), Table S1-S3 in Supplement 1).

Both CS-I and CS-II targets have more than two-orders of magnitude larger gold ACS, that is overcompensated by the (more than two-times) larger negative ACS of the gain medium, as a result the total ACS has more than two-orders of magnitude larger negative value, than the total ACS of the passive CS implanted target. Similarly, the NR-I and NR-II target has less than and almost two orders of magnitude larger gold absorption cross-section, that is overcompensated by the (more than two-times and seven-times) larger negative ACS of the gain medium, as a result the total ACS has less than two and almost three orders of magnitude larger negative value, compared to the total ACS of the NR implanted passive target (Fig. 1,2(g),(h), Table S1, S2 in Supplement 1).

Both CS-I and CS-II targets have SCS that is almost three orders of magnitude larger than the SCS in the corresponding passive target, moreover it is slightly larger than the total ACS. As a result both targets have a positive ECS throughout the inspected E_{pump} interval, that is two-times and 1.6-times larger than the ECS of the passive target at the inspected pump strength in CS-I and CS-II targets, respectively (Fig. 1(g),(h), Table S1, S2 in Supplement 1).

Similarly, the NR-I and NR-II have SCS that is more than two and three orders of magnitude larger than the SCS in the corresponding passive target, moreover it is slightly larger than the total ACS. As a result both targets have a tiny positive ECS throughout the inspected E_{pump} interval, that is 16-times and more than three-times larger in NR-I and NR-II target, than the ECS of the passive target at the inspected pump strength, respectively (Fig. 2(g),(h), Table S1, S2 in Supplement 1).

In CS-I and NR-I targets tendencies are similar, namely neither of the quantities take on global extremum (except the ACS_{gold} in CS-I), the ACS_{gold} monotonously increases in NR-I target, while the ACS_{gain} and ACS_{total} monotonously decreases. The CS-I target shows more than two-times larger absolute values of ACS ($ACS_{gold/gain/total\_CS-I} = 0.53\&0.57 \times 10^{-10}$ m^2/| -1.19×10^{-10} | m^2/|-0.66×10^{-10}| m^2 > $ACS_{gold/gain/total\_NR-I} = 0.23 \times 10^{-10}$ m^2/|-0.52×10^{-10}| m^2/|-0.29×10^{-10}| m^2). The SCS gradually increases, it is commensurate with and slightly larger than the ACS_{total}, and it is almost two-times larger for CS-I than for NR-I target ($SCS_{CS-I} = 0.67 \times 10^{-10}$ m^2> $SCS_{NR-I} = 0.37 \times 10^{-10}$ m^2). As a result, the ECS monotonously increases in CS-I, exhibits a local maximum in NR-I, but it is almost zero and positive throughout the complete E_{pump} interval. The ECS is almost an order of magnitude smaller ($ECS_{CS-I} = 0.01 \times 10^{-10}$ m^2 < $ECS_{NR-I} = 0.08 \times 10^{-10}$ m^2) in case of the CS-I target. This indicates that the CS-I target better approximates the spasing operation region, than the NR-I (Fig. 1,2(c),(g) and (d),(h), Table S1, S3 in Supplement 1).

In CS-II and NR-II target global extrema appear at 4×10^6 V/m and 3×10^6 V/m E_{pump} in all optical cross-sections. The larger gold ACS ($ACS_{gold\_CS-II} = 0.43 \times 10^{-10}$ m^2 > ACS_{gold_NR-II} = 0.37×10^{-10} m^2) and the more than two-times smaller gain medium ACS (ACS_{gain_CS-II} = |-1.07×10^{-10}| m^2 < ACS_{gain_NR-II} = |-2.71×10^{-10}| m^2) allows almost four-times smaller total ACS (ACS_{total_CS-II} = |-0.64×10^{-10}| m^2 < ACS_{total_NR-II} = |-2.35×10^{-10}| m^2) in the CS-II target. Global maximum appears in the SCS, that is commensurate with but is slightly larger than the global minimum in ACS_{total}, the ECS exhibits a tiny global maximum but it is almost

Optical Materials EXPRESS

zero and positive throughout the complete E_{pump} interval. The SCS is also almost four-times smaller ($SCS_{CS-II} = 0.65 \times 10^{-10}$ m^2 < $SCS_{NR-II} = 2.36 \times 10^{-10}$ m^2), the ECS becomes more than two-times smaller ($ECS_{CS-II} = 0.008 \times 10^{-10}$ m^2 < ECS_{NR-II} =0.017×10^{-10} m^2) at the global maximum. These relations indicate that the CS-II target also better approximates the spasing operation region, than the NR-II (Fig. 1,2(c),(g) and (d),(h), Table S1, S3 in Supplement 1).

The targets exhibit fundamentally different optical responses at the two inspected dye concentrations. This manifests itself in different tendencies, namely the CS-I and NR-I target exhibit monotonous optical cross-sections (except the ACS_{gold}, which exhibits a maximum in CS-I), whereas CS-II and NR-II exhibit global extrema in all optical cross-sections.

However, it is a remarkable difference between the two geometries embedded into media of different concentrations that each quantity have smaller absolute values in CS-II, whereas each (except the ECS) take on larger maximal values in NR-II, than in their lower concentration counterparts (Fig. 1,2(g),(h), Table S1, S3 in Supplement 1).

In the CS-I target a local maximum and a shoulder appears in the absorption cross-section spectrum of the gold and gain medium below 795 nm, and the effect of the coupled modes is recognizable in the shoulder preceding the global minimum in the negative total absorption cross-section as well. The SCS exhibits a larger global maximum, that allows the appearance of a tiny and wide ECS maximum embedding a shoulder at its short-wavelength-side as well. In CS-II target a global extremum with a long-wavelength-side neighboring peak appears at 795 nm in all absorption cross-sections. The values at global extremum in ACS, SCS and ECS are smaller in CS-II, than the values reached at 795 nm in CS-I target (Fig. 1(k),(l)).

The gold, gain medium and total absorption cross-section exhibit a single wide extremum near 795 nm in NR-I target as well. The SCS global maximum is considerably larger than the absolute value of the total ACS global minimum, that facilitates a global ECS maximum's appearance. In NR-II target a narrower global maximum appears in the gold absorption cross-section that takes on a value at 795 nm that is larger than in NR-I. The tiny global extremum in the gold ACS, the large narrow maximum in gain medium and total absorption cross-section are accompanied by a local extremum at 800 nm due to coupled modes. Similarly, global-local maximum pair appears in the SCS/ECS spectrum of NR-II with a larger/smaller amplitude compared to NR-I. The global extrema appearing in the optical cross-sections (except the ECS) in NR-II take on considerably larger values at 795 nm, than in NR-I (Fig. 2(k),(l), Table S1, S3 in Supplement 1).

All active targets result in a considerable optical cross-section enhancement compared to their passive counterpart. The degree of enhancement is on the level of orders of magnitude, depends on the optical cross-section quantity, on the nanoresonator composition and on the dye concentration as well. The latter results in that for both geometries similar switching occurs from monotonous tendencies in target-I to global extrema in target-II for all optical cross-sections. Single exception is the ECS that exhibits a global maximum in NR-I, which is larger than in NR-II.

In the absorption cross-section spectrum of gold nanoresonators of all inspected targets a global maximum appears at 795 nm that proves a plasmonic resonance and is accompanied by a global maximum in the absorption cross-section spectrum of the gain medium and the total target. Also, the optical cross-sections prove that in case of CS implanted targets the smaller concentration (CS-I target), whereas in case of the NR implanted targets the larger concentration (NR-II) facilitates more additional modes' coupling that result in wider spectra. The SCS outperforms the ACS, therefore the ECS exhibits a small positive global maximum, i.e. neither of the targets enters the spasing operation region in the inspected wavelength interval. The ECS better approximates zero in case of CS implantation independent of concentration (Fig. 1,2(c),(g),(k) and (d),(h),(l), Table S1-S3 in Supplement 1).

Optical Materials EXPRESS

3.4. Comparison of achieved distributions

The compared active targets are as follows: (1) CS-I that is pumped at $E_{pump} = 3 \times 10^6$ V/m and is doped with dye of 5×10^{25} m^{-3} concentration, (2) NR-I that is pumped at $E_{pump} = 3 \times 10^6$ V/m and is doped with dye of the smallest 2×10^{25} m^{-3} concentration, (3) CS-II that is pumped at larger $E_{pump} = 4 \times 10^6$ V/m **E**-field strength and is doped with dye of 2.25×10^{26} m^{-3} concentration, and (4) NR-II that is pumped at $E_{pump} = 3 \times 10^6$ V/m and is doped with dye of the highest 2.5×10^{26} m^{-3} concentration (see Supplement 1 Table S4-S9).

3.4.1. Absorption distribution

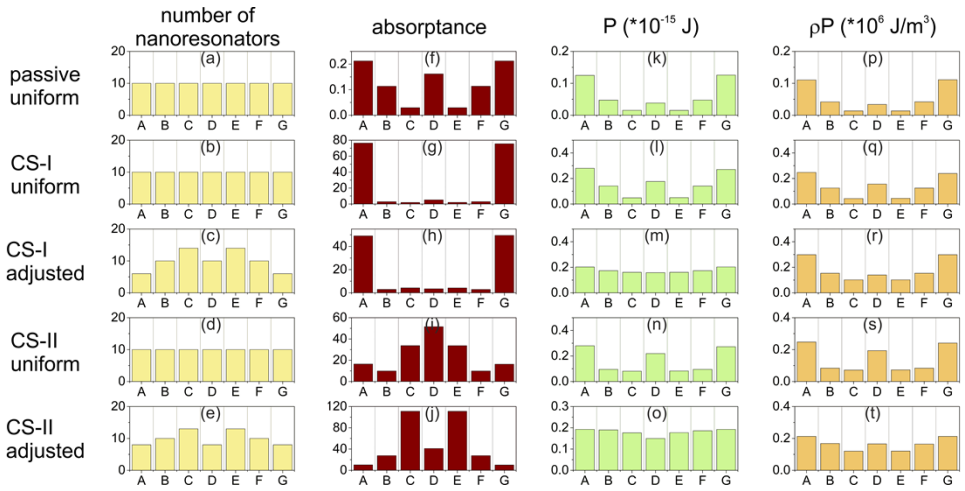

Fig. 3. Time-dependent response of the passive and active CS nanoresonator implanted targets. The (a-e) CS number density, (f-j) absorption, (k-o) power-loss and (p-t) power-loss density distribution for (a, f, k, p) uniform CS nanoresonator distribution in passive target, and (b,g,l,q/d,i,n,s and c,h,m,r/e,j,o,t) uniform and adjusted CS nanoresonator distribution in targets doped with dye at smaller (I) / larger (II) concentration.

The uniform CS and NR distribution in a passive target results in similar 0.872 and 0.825 absorptance, respectively. The absorption distribution of the inspected passive targets is similar in the sense that a local maximum appears in the central layer. The absorption decreases towards the inner layers gradually in case of CS, whereas it is uniform in the intermediate layers in case of NR implantation. The lack of an exponentially decreasing profile (that is expected from the Beer-Lambert law) is caused by the double-sided illumination and that the nanorods possess random orientation beside random location within the target. Despite the orientation independence, the CS implanted passive target has a commensurate absorptance and two-times larger standard deviation ($\delta_{A\_CS-passive} = 0.615$) than the NR implanted passive target ($\delta_{A\_NR-passive} = 0.305$) (Fig. 3 and 4(f)-(j), Table S4, S5 in Supplement 1).

All active targets result in significantly larger total absorptance than their CS and NR implanted passive counterpart. The absorbance is greater than unity because the plasmonically enhanced dye emission is captured by the nanoresonators (Table S4-S6 in Supplement 1).

The absorption distribution is similar in the CS-I and NR-I targets doped with dye of smaller concentration (Fig. 3 and 4(g)). By comparing the absorption distribution of the passive and active targets, the effect of dye doping is that the absorption increases significantly in the nanoresonators, and the increase is the largest, where the probe field enters the target. As a consequence, most of the absorption is concentrated in the outermost layers. The absorption gradually decreases

Optical Materials EXPRESS

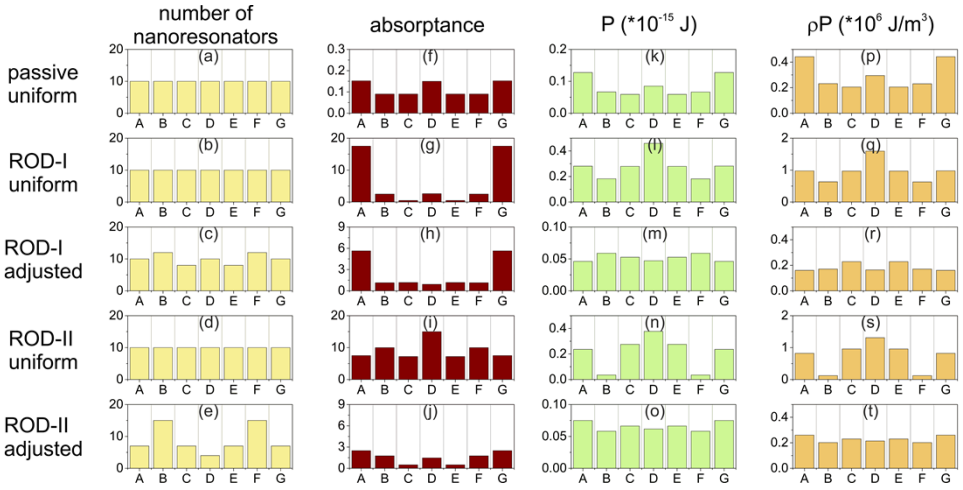

Fig. 4. Time-dependent response of the passive and active NR nanoresonator implanted targets. The (a-e) NR number density, (f-j) absorption, (k-o) power-loss and (p-t) power-loss density distribution for (a, f, k, p) uniform NR nanoresonator distribution in passive target, and (b,g,l,q/d,i,n,s and c,h,m,r/e,j,o,t) of uniform and adjusted NR nanoresonator distribution in targets doped with dye at smaller (I) / larger (II) concentrations.

towards the inner layers, but a local maximum appears in the central layer, similarly to the passive target, but with a relatively smaller modulation amplitude compared to target edge.

Dye doping of the CS and NR implanted polymer target with smaller concentration results in an absorptance with more than (191.5-fold) and almost (53.7-fold) two orders of magnitude larger value ($A_{CS-I} = 166.99 > A_{NR-I} = 44.3$) compared to the passive counterpart at a cost of more than two-times and four-times larger standard deviation ($\delta_{A\_CS-I} = 1.493 > \delta_{A\_NR-I} = 1.259$) in CS-I and NR-I target, respectively. In CS-I the total absorptance is almost four-times larger than in NR-I target, however the standard deviation is also larger in CS-I than in NR-I target (Table S4-S7 in Supplement 1).

The adjustment results in an absorption increase, a local minimum appears at the center of both type-I targets, preceded by an increase from an equal value in CS-I and by a larger layer-independent value in NR-I target (Fig. 3 and 4(h)). The high absorption in the outermost layers indicates that the absorption is unbalanced. As a result of adjustment more than two /one order of magnitude larger absorptance with two-times /three-times larger deviation is achievable in CS-I /NR-I target compared to their passive counterparts. After adjustment the total absorption ($A_{CS-I\_adj} = 116.4 > A_{NR-I\_adj} = 16.8$) indicates a decrease by a factor of 0.70× for CS-I and by a factor of 0.38× for NR-I nanoresonator distribution compared to the counterpart uniform distribution. The adjustment decreases not only the absorption, but also its standard deviation ($\delta_{A\_CS-I\_adj} = 1.343 > \delta_{A\_NR-I\_adj} = 0.922$), however only the latter is advantageous in reaching large and uniform energy deposition. The adjusted distribution in CS-I exhibits almost seven-times larger absorption, but the standard deviation of absorption is also larger, than in case of adjusted distribution in NR-I target. The adjustment does not modify the absorption and standard deviation relations between targets implanted with different nanoresonator types (Table S4-S8 in Supplement 1).

The absorption distributions are different in CS-II and NR-II implanted targets doped with dye of larger concentration (Fig. 3 and 4(i)). The global maximum of the absorption distribution is at the center of the target in both cases. In the intermediate layers there are symmetrically aligned

Optical Materials EXPRESS

local minima in the CS-II target, whereas symmetrically arranged local maxima appear in the NR-II target.

Dye doping of the polymer target at larger concentration results in a more than (196.48-fold) and almost (76.34-fold) two orders of magnitude larger absorptance ($A_{CS-II} = 171.34 > A_{NR-II} = 62.98$) in CS-II and NR-II target compared their passive counterparts, respectively. The degree of absorption increase is similar to the type-I targets, moreover, the standard deviation of absorptance ($\delta_{A\_CS-II} = 0.638 > \delta_{A\_NR-II} = 0.318$) significantly better approaches the value achieved in the CS and NR implanted passive targets, which is advantageous. The total absorptance is almost three-times larger, but the standard deviation is also two-times larger in CS-II target compared to the NR-II. The CS-II target results in larger total absorptance with a less uniform distribution than the NR-II target, similarly to the targets doped with dye of smaller concentration (Table S4-S7).

The absorption in adjusted distributions in CS-II and NR-II targets exhibits a local minimum and maximum at the target center, preceded by a symmetrically arranged maximum and minimum that are inserted into layers with monotonously increasing and decreasing absorption tendencies, respectively (Fig. 3 and 4(j)). After adjustment the absorption is more than two / one order of magnitude larger with 1.5/1.7-times larger standard deviation in CS-II /NR-II targets, compared to their passive counterparts. After adjustment the absorption modifies nanoresonator geometry dependently in targets doped with larger concentration of dye, namely the value ($A_{CS-II\_adj} = 338.47 > A_{NR-II\_adj} = 10.95$) becomes larger by a factor of 1.98× in CS-II and smaller by a factor of 0.17× in NR-II target, compared to the uniform distribution. The adjustment results in absorption and standard deviation increase in CS-II, while a decreased absorption is accompanied by an increased standard deviation in NR-II ($\delta_{A\_CS-II\_adj} = 0.913 > \delta_{A\_NR-II\_adj} = 0.528$), which is a disadvantage. In the case of adjusted distribution in CS-II target the maximal absorption is more than thirty-times larger, but the standard deviation is also almost two-times larger, than in NR-II target. The adjustment preserves the absorption and standard deviation relations between targets implanted with different nanoresonator types also in case of doping with dye of larger concentration (Table S4-S8 in Supplement 1).

3.4.2. Comparison of the effects of media, distributions, dye concentrations and nanoresonator geometries on the absorption distribution

The qualitative comparison of uniform nanoresonator distributions shows that the increase in the dye concentration results in an increase in absorption not only in the outer layers (except where the probe field enters the target), but also in the inner layers that leads to higher absorption with a more uniform distribution independently of nanoresonator geometry. As a result, by increasing the dye concentration, the absorption increases and the uniformity better approaches that of absorption distribution in the passive targets for both nanoresonator geometries. The total absorption is larger by a factor of 1.03× and 1.42×, while the standard deviation is more than two-times and almost four-times smaller for the type-II targets implanted with uniform distributions of CS and NR nanoresonators, respectively (Table S9 in Supplement 1).

The qualitative comparison shows that the nanoresonator distribution adjustment at larger dye concentration better preserves the increased absorption in the inner layers and more efficiently decreases it in the outer layers, nanoresonator independently. The global maxima in the layers neighboring the central one promote the absorption increase in CS-II, whereas the local minima at the half of the targets limit the absorption increase in NR-II, compared to their smaller concentration counterparts. By realizing the adjustment at higher dye concentration the absorption increase (decrease) is accompanied by better uniformity in case of CS (NR) nanoresonator distributions, respectively. In presence of the adjusted distribution in CS-II the absorption is larger by a factor of 2.91× and the standard deviation is smaller by a factor of 0.68×, while in presence of the adjusted distribution in NR-II the absorption and standard deviation is

Optical Materials EXPRESS

smaller by a factor of 0.65× and 0.57×, respectively, compared to the adjusted distribution in counterpart type-I targets (Table S9 in Supplement 1).

All active targets result in significantly larger total absorptance than their CS and NR implanted passive counterpart, however the degree of enhancement depends on the dye concentration. The adjustment with the purpose of power-loss balancing decreases the absorption, but is accompanied by improved uniformity of the absorption in CS-I and NR-I targets. After adjustment the absorption increase in CS-II and absorption decrease in NR-II is accompanied by standard deviation increase. The absorption is four- (three-) times and almost (more than) an order of magnitude larger, while the absorption distribution is less uniform both in the uniform and adjusted distributions in CS-I(II) target than in NR-I(II) target.

By increasing the dye concentration in the active targets, the uniformity of absorption distribution is better for both nanoresonator geometries, both for uniform and adjusted distributions. The adjustment is more (less) efficient in absorption enhancement inside inner layers in case of CS (NR) nanoresonator geometry. The advantage of the CS is the larger absorption, which can be further enhanced via adjustment – but the drawback is the larger standard deviation.

3.4.3. Power-loss and power-loss density distribution

For the passive target, the absorption, power-loss (P) and power-loss density (ρP) distributions are correlating, independently of the implanted nanoresonator geometry. The uniform CS and NR distributions in passive targets result in similar power-loss and power-loss density distribution in the nanoresonators. The power-loss (power-loss density) is 4.14×10^{-16} J (7.36×10^{-16} J) (5.23×10^{4} J/m^3 (9.29×10^{4} J/m^3)) and 2.13×10^{-16} J (1.06×10^{5} J/m^3) for the CS and NR implantation in case of 3×10^{6} V/m (4×10^{6} V/m) pump **E**-field amplitude, respectively. The uniformity of the power-loss distributions throughout the targets differs, the CS implanted passive target exhibits more than two-times larger standard deviation ($\delta_{P\_CS-passive} = 0.798$) than the NR implanted passive target ($\delta_{P\_NR-passive} = 0.365$)) in both quantities, similarly to the absorption (Fig. 3 and 4(a),(f),(k),(p), Table S4, S5 in Supplement 1).

All active targets result in significantly larger power-loss and power-loss density than their CS and NR implanted passive counterpart.

The power-loss integrated until the short pulses overlap is improved, since the plasmonically enhanced dye emission is captured by the nanoresonators already during the short laser pulse (Table S4-S6 in Supplement 1).

The power-loss and power-loss density distributions correlate with the absorption distribution in case of CS-I target but with a relatively larger local maximum in the middle layer. In contrast, the power-loss and power-loss density in NRs do not correlate with the absorption distribution for the NR-I target. The highest power-loss and power-loss density is taken on at the middle of the target rather than in the outermost layers and a drop occurs in the intermediate layers. There is a symmetrically arranged minimum-pair in the intermediate layers, while the global maximum in power-loss and power-loss density in the middle layer is almost three-times larger than the local minimum in the intermediate layers (Fig. 3,4(b),(g),(l),(q), please see energy and energy density distribution in Supplement 1 Figure S1,S2(b),(g),(l),(q)).

The power-loss ($P_{CS-I} = 1.11\times10^{-15}$ J $< P_{NR-I} = 1.94\times10^{-15}$ J) is higher than without dye doping in CS-I and NR-I targets. According to the uniform nanoresonator distribution, the power-loss density consistently follows the power-loss distribution with an accumulated value of ($\rho P_{CS-I} = 1.4\times10^{5}$ J/m^3 $< \rho P_{NR-I} = 9.65\times10^{5}$ J/m^3), which is larger than that of the counterpart passive target. Both the power-loss and power-loss density values vary by a factor of almost 3× / 9× compared to the values achieved via uniform distribution in the passive CS-I/NR-I target. For type-I targets the power-loss and power-loss density distribution is more uniform than in the passive target implanted with CS and NR ($\delta_{P\_CS-I} = \delta_{\rho P\_CS-I} = 0.589 > \delta_{P\_NR-I} = \delta_{\rho P\_NR-I} = 0.332$) (Table S4-S6 in Supplement 1). By comparing CS-I and NR-I targets the power-loss is almost two-times

Optical Materials EXPRESS

(0.57×) and the power-loss density is almost seven-times smaller, but the standard deviation is also (1.77×) larger for both quantities in CS-I target. The CS-I target results in smaller power-loss and power-loss density with less uniform distribution in both quantities than the NR-I target, indicating that this configuration is less suitable for efficient uniform energy deposition (Fig. 3,4(b),(g),(l),(q), Table S4-S7 in Supplement 1).

The adjustment of nanoresonator distribution in CS-I results in monotonously decreasing power-loss distribution toward the center, whereas a tiny local maximum appears in its density at the middle of the target (Fig. 3 (m),(r)). The adjustment of nanoresonator distribution in NR-I results in power-loss as well as power-loss density distributions that shows a symmetrically arranged maximum pair. The value at the middle is as large as the values in the outermost layers. The global power-loss maxima are taken on in the layers neighboring the outermost ones, while its density is maximal in the layers neighboring the central one (Fig. 4(m),(r)).

The power-loss ($P_{CS-I\_adjusted} = 1.23 \times 10^{-15}$ J > $P_{NR-I\_adjusted} = 3.63 \times 10^{-16}$ J) achieved via adjusted distribution is slightly larger / significantly smaller compared to the value reached via uniform distribution in CS-I /NR-I target. According to the adjusted (non-uniform) nanoresonator distribution, the average power-loss density distribution differs from the power-loss distribution with an accumulated value of ($\rho P_{CS-I\_adjusted} = 1.55 \times 10^5$ J/m^3 < $\rho P_{NR-I\_adjusted} = 1.8 \times 10^5$ J/m^3), which is slightly larger /significantly smaller than that of the uniform distribution. Both the power-loss and power-loss density values vary by a factor of 1.11× / 0.19× compared to the values achieved via uniform distribution in CS-I/NR-I target. For adjusted nanoresonator distributions in type-I targets the power-loss (power-loss density) distribution is more uniform than for the uniform distribution of CS and NR ($\delta_{P\_CS-I\_adjusted} = 0.109 \sim \delta_{P\_NR-I\_adjusted} = 0.108$ ($\delta_{\rho P\_CS-I\_adjusted} = 0.478 > \delta_{\rho P\_NR-I\_adjusted} = 0.163$)) (Table S4-S8 in Supplement 1). By comparing the adjusted distributions in CS-I and NR-I targets the power-loss is more than three-times larger for CS-I target, and the standard deviation is almost the same. The power-loss density is smaller (0.86×), moreover the standard deviation is almost three-times larger for CS-I target. The CS-I target results in larger power-loss with the same standard deviation indicating that it is more advantageous, although it exhibits smaller power-loss density with larger standard deviation than the NR-I target.

The adjustment reverses the power-loss relations, balances its standard deviation between CS-I and NR-I targets, while the power-loss density and standard deviation relations are preserved (Table S4-S7 in Supplement 1).

The distribution of power-loss and power-loss density in CS-II and NR-II target doped with dye of larger concentration is similar to that in CS-I and NR-I target. The only difference is that in CS-II the symmetrically arranged minima are more /less deeper, since the decrease is more /less rapid from the outermost layers, while in NR-II difference appears between the values neighboring the local minima (Fig. 3,4(d),(i),(n),(s)).

The power-loss ($P_{CS-II} = 1.12 \times 10^{-15}$ J < $P_{NR-II} = 1.47 \times 10^{-15}$ J) is larger than without dye doping both in CS-II and NR-II targets. According to the uniform nanoresonator distribution, the power-loss density consistently follows the power-loss distribution with an accumulated value of ($\rho P_{CS-II} = 1.41 \times 10^5$ J/m^3 < $\rho P_{NR-II} = 7.32 \times 10^5$ J/m^3), which is larger than that of the passive target. Both the power-loss and power-loss density vary by a factor of 1.5× /almost 7× compared to the values achieved via uniform distribution in passive CS-II/NR-II target (Table S6 in Supplement 1).

For type-II targets the power-loss distribution is more (less) uniform than the power-loss distribution in the passive target with CS (NR) implantation ($\delta_{P\_CS-II} = 0.576 = \delta_{\rho P\_CS-II} < \delta_{P\_NR-II} = \delta_{\rho P\_NR-II} = 0.611$) (Table S4-S6). In CS-II the power-loss (0.76×), while the power-loss density is more than five-times smaller (0.19×), and the standard deviation is also slightly (0.94×) smaller for both quantities, than in NR-II target. The CS-II target results in smaller total power-loss and power-loss density values with a slightly more uniform distribution than the NR-II target

Optical Materials EXPRESS

indicating that it is weaker in power-loss enhancement but slightly better in power-loss distribution uniformity improvement (Fig. 3,4(d),(i),(n),(s), Table S4-S7 in Supplement 1).

The adjustment of nanoresonator distribution in CS-II target results in monotonously decreasing power-loss distribution, whereas a tiny local maximum appears in its density at the middle of the target, similarly to the CS-I target (Fig. 3(e),(j),(o),(t)). The adjustment of nanoresonator distribution in NR-I results in power-loss and power-loss density distributions that show a symmetrically arranged minimum pair, this characteristic is more likely to that of the uniform distribution, in contrast to NR-I target. The value at the middle is as large as the values at the local minimum, which also differs from the NR-I target. The global maxima are taken on in the outermost layers both in power-loss and in power-loss density (Fig. 4(e),(j),(o),(t)).

The power-loss ($P_{CS-II} = 1.26 \times 10^{-15}$ J > $P_{NR-II} = 4.6 \times 10^{-16}$ J) achieved via adjusted nanoresonator distribution is slightly larger / significantly smaller compared to the value reached via uniform distribution in CS-II / NR-II target. According to the adjusted (non-uniform) nanoresonator distribution, the average power-loss density differs from the power-loss distribution with an accumulated value of ($\rho P_{CS-II} = 1.59 \times 10^5$ J/m^3 < $\rho P_{NR-II} = 2.29 \times 10^5$ J/m^3), which is slightly larger / significantly smaller than that of the uniform distribution. Both the power-loss and power-loss density vary by a factor of 1.13× / 0.31× compared to the values achieved via uniform distribution in CS-I/NR-I target. For adjusted distributions in type-II targets the power-loss (power-loss density) distribution is more uniform than for uniform CS (NR) distribution ($\delta_{P\_CS-II\_adjusted} = 0.084 < \delta_{P\_NR-II\_adjusted} = 0.108$ ($\delta_{\rho P\_CS-II} = 0.\ 227 < \delta_{\rho P\_NR-II} = 0.\ 459$) (Table S4-S8 in Supplement 1).

The power-loss is almost three-times larger, moreover its standard deviation is smaller (0.74×), while the power-loss density is smaller (0.69×), and its standard deviation is also smaller (0.49×) in CS-II than in NR-II target. The CS-II target results in larger total power-loss and smaller power-loss density values with more uniform distributions than the NR-II target proving that it is better in power-loss enhancement and uniformity improvement. The adjustment reverses the power-loss relations between targets implanted with different nanoresonator types, but the power-loss density and standard deviation relations are preserved (Fig. 3,4(e),(j),(o),(t)), Table S4-S7 in Supplement 1).

3.4.4. Comparison of the effects of media, distributions, dye concentrations and nanoresonator geometries on the power-loss distribution

The qualitative comparison shows that the increase in dye concentration around uniformly distributed nanoresonators results in more rapid decrease and allows more similar intermediate values in case of CS, but causes different neighboring values in case of NR implantation.

By quantitatively comparing the uniform distributions in type-I and type-II active targets the power-loss and power-loss density are slightly larger for CS-II, and the standard deviation is slightly smaller compared to CS-I target for both quantities. In contrast, in case of uniform distribution of NR both quantities are smaller, moreover the standard deviation is considerably larger in NR-II compared to the NR-I target. Namely, for type-II targets implanted with uniform distribution of nanoresonators the power-loss becomes larger by a factor of 1.01×, while the standard deviation is smaller by factor of 0.98× for CS, but for NR it is smaller by a factor of 0.76×, while the standard deviation is larger by a factor of 1.84× (Table S9, Supplement 1).

The qualitative comparison shows that the adjustment of nanoresonators at larger dye concentration results in monotonous power-loss decrease towards the target center without inserted local maximum in case of CS composition, whereas it results in two side minima instead of two side maxima in power-loss for NR implantation.

By quantitatively comparing the adjusted distribution in type-I and type-II active targets all relations are preserved for the CS nanoresonator, moreover the power-loss and its density is further enhanced and the standard deviation is more efficiently reduced. In contrast, in case of NR

Optical Materials EXPRESS

geometry by increasing the concentration the power-loss and power-loss density also becomes larger, the standard deviation of power-loss reaches the same value, but it becomes larger for the power-loss density. Namely, the power-loss becomes larger by a factor of 1.02× while the standard deviation becomes smaller by a factor of 0.77× for CS, and it is larger by a factor of 1.27×, but the standard deviation remains the same for NR, in the II-type targets with adjusted distributions of nanoresonators (Table S9).

All active targets implanted with uniform distribution of nanoresonators result in larger power-loss and power-loss density than their passive counterparts with smaller (smaller/larger) standard deviation for CS (NR-I/NR-II). By adjusting the nanoresonator distribution, the power-loss and power-loss density increase (decrease) in case of CS (NR implantation), while the standard deviation become smaller for both geometries and for both concentrations (Table S6, S9, Supplement 1).

By increasing the dye concentration in the active targets, the power-loss and power-loss density increase (decrease in uniform and increase in adjusted distribution), while the standard deviation becomes smaller (larger except the power-loss in the adjusted distribution that remains the same) in case of CS (NR) implantation. The advantage of the higher concentration in larger power-loss and smaller standard deviation achievement is nanoresonator geometry dependent, and manifests itself in both quantities in CS-II and in the power-loss and power-loss density increase in presence of the adjusted distribution in NR-II target.

4. Conclusion

At the inspected E_{pump} – dye concentration parameters, both for core-shell (CS) and nanorod (NR) distributions the achieved **E**-field maximum is higher in the targets doped with dye of smaller concentration (type-I targets) than in the targets doped with dye of larger concentration (type-II targets), whereas the optical responses and cross-sections take on larger values and the spectral responses exhibit various coupled modes in CS-I and NR-II targets.

Targets implanted with CS composition nanoresonators better approximate the spasing operation, as indicated by the smaller extinction cross-section at both inspected dye concentrations. The CS nanoresonator implantation in active targets allows larger absorption at a cost of larger standard deviation. Dye doping in CS (NR)-I/II targets results in huge (moderate) steady-state absorption increase and is accompanied by standard deviation increase. When the target is doped with dye of larger concentration, larger value (except the adjusted NR-II) and smaller standard deviation of absorption is achievable.

Larger total deposited power-loss and power-loss density are achieved in presence of uniform distributions in type-I and II active targets, than in their corresponding passive counterpart, independently of nanoresonator geometry. The uniform nanoresonator distributions result in more (more/less) uniform power-loss and power-loss density distribution in active CS-I and CS-II (NR-I/II) targets, than in their passive counterparts.

The adjustment is accompanied by standard deviation decrease of absorption in CS-I and NR-I, and by absorption increase in CS-II target. Larger power-loss and power-loss density are achieved in presence of adjusted distributions in CS-I and CS-II active targets than in their uniform counterparts. In contrast, in presence of adjusted distributions both quantities become smaller compared to the uniform distributions in NR-I and NR-II targets. The standard deviation becomes smaller for both quantities independent of nanoresonator geometry, indicating that for both type-I and type-II targets implanted with adjusted nanoresonator distributions the power-loss and power-loss density distributions are more uniform than in case of uniform CS (NR) distribution. This proves that the realized nanoresonator distribution adjustment to increase energy deposition uniformity is successful.

Optical Materials EXPRESS

As a result of adjustment, the power-loss becomes larger beside the commensurately and better reduced standard deviation in CS-I and CS-II target, indicating that the adjusted core-shell nanoresonator distributions outperform the nanorod ones at both concentrations.

The larger dye concentration allows larger power-loss and power-loss density values with smaller standard deviation in presence both of uniform and adjusted CS distributions. In contrast, in case of NR only the adjusted distribution allows increase in values with increasing dye concentration, but it is accompanied by the same balanced standard deviation only in power-loss. Based on the results the adjusted distributions of CS nanoresonators in targets doped with dye of higher concentration are proposed to achieve uniform absorbed power-loss distribution.

These results demonstrate that by optimizing the distribution of the plasmonic nanoresonators and on demand the dye concentration, four dimensional control of light-matter interaction can be realized in various active media, even in nonlinear regime. In optimized fusion targets, where the plasmonic nanoresonators designation is the boosting of the local **E**-field, extremely large field strengths can be achieved throughout macroscopic regions, and uniform ignition can be achieved before the damage and saturation phenomena set on longer time-scales. At such extreme field intensities application of hydrodynamic models is necessary, considering that the non-linear susceptibility is nanoparticle and pulse characteristic dependent. Uniform **E**-field enhancement maximization to control ultra-strong light-matter interactions in extended targets is a subject of ongoing studies.

Funding. Norges Forskningsråd (255253); Eötvös Lóránd Research Network of Hungary; Nemzeti Kutatási Fejlesztési és Innovációs Hivatal (NKFIH-468–3/2021); Nemzeti Kutatási Fejlesztési és Innovációs Hivatal ("Optimized nanoplasmonics" K116362).

Acknowledgments. Enlightening discussions with Professor Johann Rafelski are gratefully acknowledged. This is a NAPLIFE Collaboration.

Disclosures. The authors declare no conflicts of interest.

Data availability. Data underlying the results presented in this paper may be obtained from the authors upon reasonable request.

Supplemental document. See Supplement 1 for supporting content.

References

1. K. Tanabe, *Plasmonics for Hydrogen Energy* (Springer, 2022).
2. M. A. Purvis, V. N. Shlyaptsev, R. Hollinger, C. Bargsten, A. Pukhov, A. Prieto, Y. Wang, B. M. Luther, L. Yin, S. Wang, and J. J. Roca, "Relativistic plasma nanophotonics for ultrahigh energy density physics," Nat. Photonics **7**(10), 796–800 (2013).
3. D. Duffit, A. Rosenfeld, S. K. Das, R. Grunwald, and J. Bonse, "Femtosecond laser-induced periodic surface structures revisited: A comparative study on ZnO," J. Appl. Phys. **105**(3), 034908 (2009).
4. A. Lübcke, A. A. Andreev, S. Höhm, R. Grunwald, L. Ehrentraut, and M. Schnürer, "Prospects of target nanostructuring for laser proton acceleration," Sci. Rep. **7**(1), 44030 (2017).
5. G. Pirruccio, D. Rocco, C. De Angelis, G. Sorbello, D. Mascali, G. Torrisi, M. Frassetto, L. Malferrari, F. Odorici, C. Altana, G. Lanzalone, A. Muoio, S. Tudisco, R. Benocci, G. Gorini, and L. Palladino, "Numerical simulations on laser absorption enhancement in hybrid metallo-dielectric nanostructured targets for future nuclear astrophysics experiments," AIP Adv. **10**(4), 045020 (2020).
6. N. Fukuoka and K. Tanabe, "Lightning-rod effect of plasmonic field enhancement on hydrogen-absorbing transition metals," Nanomaterials **9**(9), 1235 (2019).
7. C. F. Bohren and D. R. Huffman, *Absorption and Scattering of Light by Small Particles* (Wiley, 1998).
8. C. Noguez, "Surface plasmons on metal nanoparticles: the influence of shape and physical environment," J. Phys. Chem. C **111**(10), 3806–3819 (2007).
9. X. Huang, S. Neretina, and M. A. El-Sayed, "Gold nanorods: from synthesis and properties to biological and biomedical applications," Adv. Mater. **21**(48), 4880–4910 (2009).
10. H. Ma, P. M. Bendix, and L. B. Oddershede, "Large-scale orientation dependent heating from a single irradiated gold nanorod," Nano Lett. **12**(8), 3954–3960 (2012).
11. I. Pastozira-Santos, C. Kinnear, J. Pérez-Juste, P. Mulvaney, and L. M. Liz-Marzán, "Plasmonic polymer nanocomposites," Nat. Rev. Mater. **3**(10), 375–391 (2018).
12. E. Prodan, C. Radloff, N. J. Halas, and P. Nordlander, "A hybridization model for the plasmon response of complex nanostructures," Science **302**(5644), 419–422 (2003).

Optical Materials EXPRESS

13. N. J. Halas, "Playing with plasmons: tuning the optical resonant properties of metallic nanoshells," MRS Bull. **30**(5), 362–367 (2005).
14. A. M. Goodman, N. J. Hogan, S. Gottheim, C. Li, S. E. Clare, and N. J. Halas, "Understanding resonant light-triggered DNA release from plasmonic nanoparticles," ACS Nano **11**(1), 171–179 (2017).
15. J. Morales-Dalmau, C. Viclhes, I. de Miguel, V. Sanz, and R. Quidant, "Optimum morphology of gold nanorods for light-induced hyperthermia," Nanoscale **10**(5), 2632–2638 (2018).
16. G. Baffou, F. Cichos, and R. Quidant, "Applications and challenges of thermoplasmonics," Nat. Mater. **19**(9), 946–958 (2020).
17. J. A. Schuller, E. S. Barnard, W. Cai, Y. C. Jun, J. S. White, and M. L. Brongersma, "Plasmonics for extreme light concentration and manipulation," Nat. Mater. **9**(3), 193–204 (2010).
18. M. Pelton, J. Aizpurua, and G. Bryant, "Metal-nanoparticle plasmonics," Laser Photonics Rev. **2**(3), 136–159 (2008).
19. E. Cubucku, N. Yu, E. J. Smythe, L. Diehl, K. B. Crozier, and F. Capasso, "Plasmonic laser antennas and related devices," IEEE J. Sel. Top. Quantum Electron. **14**(6), 1448–1461 (2008).
20. K. E. Dorfman, P. K. Jha, D. V. Voronine, P. Genevet, F. Capasso, and M. O. Scully, "Quantum-coherence-enhanced surface plasmon amplification by stimulated emission of radiation," Phys. Rev. Lett. **111**(4), 043601 (2013).
21. M. A. Noginov, G. Zhu, A. M. Belgrave, R. Bakker, V. M. Shalaev, E. E. Narimanov, S. Stout, E. Herz, T. Suteewong, and U. Wiesner, "Demonstration of a spaser-based nanolaser," Nature **460**(7259), 1110–1112 (2009).
22. N. Arnold, C. Hrelescu, and T. A. Klar, "Minimal spaser threshold within electrodynamic framework: shape, size and modes," Ann. Phys. **528**(3-4), 295–306 (2016).
23. A. Szenes, D. Vass, B. Bánhelyi, and M. Csete, "Active individual nanoresonators optimized for lasing and spasing operation," Nanomaterials **11**(5), 1322 (2021).
24. A. Yang, D. Wang, W. Wang, and T. W. Odom, "Coherent light sources at the nanoscale," Annu. Rev. Phys. Chem. **68**(1), 83–99 (2017).
25. R.-M. Ma and R. F. Oulton, "Applications of nanolasers," Nat. Nanotechnol. **14**(1), 12–22 (2019).
26. Z. Wang, Z. Kan, and M. Shen, "Study the plasmonic property of gold nanorods highly above damage threshold via single-pulse spectral hole-burning experiments," Sci. Rep. **11**(1), 22232 (2021).
27. I. Papp, L. Bravina, M. Csete, A. Kumari, I. N. Mishustin, D. Molnár, A. Motornenko, P. Rácz, L. M. Satarov, H. Stöcker, D. D. Strottman, A. Szenes, D. Vass, T. S. Bíró, L. P. Csernai, N. Kroó, and NAPLIFE Collaboration, "Kinetic model evaluation of the resilience of plasmonic nanoantennas for laser-induced fusion," PRX Energy **1**(2), 023001 (2022).
28. A. Yadav, L. Zhong, J. Sun, L. Jiang, G. J. Cheng, and L. Chi, "Tunable random lasing behavior in plasmonic nanostructures," Nano Convergence **4**(1), 1 (2017).
29. X. Meng, K. Fujita, Y. Moriguchi, Y. Zong, and K. Tanaka, "Metal–dielectric core–shell nanoparticles: advanced plasmonic architectures towards multiple control of random lasers," Adv. Opt. Mater. **1**(8), 573–580 (2013).
30. Z. Wang, X. Meng, A. V. Kildishev, A. Boltasseva, and V. M. Shalaev, "Nanolasers enabled by metallic nanoparticles: from spasers to random lasers," Laser Photonics Rev. **11**(6), 1700212 (2017).
31. K. Tanabe, "Plasmonic energy nanofocusing for high-efficiency laser fusion ignition," Jpn. J. Appl. Phys. **55**(8S3), 08RG01 (2016).
32. K. Tanabe, "Plasmonic concepts for condensed matter nuclear fusion," J. Condens. Matter Nucl. Sci. **24**, 296–300 (2017).
33. L. P. Csernai, M. Csete, I. N. Mishustin, A. Motornenko, I. Papp, L. M. Satarov, H. Stöcker, N. Kroó, and NAPLIFE Collaboration, "Radiation-dominated implosion with flat target," Phys. Wave Phen. **28**(3), 187–199 (2020).
34. L. P. Csernai, N. Kroó, and I. Papp, "Radiation dominated implosion with nano-plasmonics," Laser Part. Beams **36**(2), 171–178 (2018).
35. M. Csete, A. Szenes, E. Tóth, D. Vass, O. Fekete, B. Bánhelyi, I. Papp, T. Bíró, L. P. Csernai, N. Kroó, and NAPLIFE Collaboration, "Comparative study on the uniform energy deposition achievable via optimized plasmonic nanoresonator distributions," Plasmonics **17**(2), 775–787 (2022).
36. A. M. Fales, W. C. Vogt, T. J. Pfefer, and I. K. Ilev, "Quantitative evaluation of nanosecond pulsed laser-induced photomodification of plasmonic gold nanoparticles," Sci. Rep. **7**(1), 15704 (2017).
37. C. Kern, M. Zürch, J. Petschulat, T. Pertsch, B. Kley, T. Käsebier, U. Hübner, and C. Spielmann, "Comparison of femtosecond laser-induced damage on unstructured vs. nano-structured Au-targets," Appl. Phys. A **104**(1), 15–21 (2011).
38. B. J. Nagy, Z. Pápa, L. Péter, C. Prietl, J. R. Krenn, and P. Dombi, "Near-field-induced femtosecond breakdown of plasmonic nanoparticles," Plasmonics **15**(2), 335–340 (2020).
39. P. Ginzburg, A. V. Karsavin, G. A. Wurtz, and A. V. Zayats, "Nonperturbative hydrodynamic model for multiple harmonics generation in metallic nanostructures," ACS Photonics **2**(1), 8–13 (2015).
40. A. M. M. Gherman, N. Tosa, D. N. Dadarlat, V. Tosa, M. V. Cristea, and P. S. Agachi, "Temperature dynamics of laser irradiated gold nanoparticles embedded in a polymer matrix," Thermochim. Acta **656**, 25–31 (2017).

160.114.23.240 {ts '2023-04-21 03:38:41'}